Modeling of Lung Nodules from LDCT of the Human Chest: Algorithms and Evaluation for CAD Systems

Amal A. Farag, Mostafa Farag, James Graham, Salwa Elshazly, Mohamed al Mogy and Aly Farag

Abstract This chapter provides a complete model-based approach for analysis of lung nodules visibly observed in clinical low dose CT (LDCT) scans of the human chest. The purpose is to highlight elements of computer-assisted diagnosis (CAD) software that can be validated using multiple radiologists using modern computing and information technology. The front-end components of the proposed approach are the following: lung nodule modeling, nodule detection, nodule segmentation, and CAD system design and evaluation. The implicit steps involved in developing these components, include filtering of the LDCT scans to reduce noise artifacts and other uncertainties associated with the imaging protocol; segmentation of the lung tissue from the rest of organs appearing in the LDCT of the chest; and creating an ensemble of nodules by human experts. As nodules take various shapes, sizes and pathologies, we limit our treatment to small size nodule ≤ 1 cm in diameter. Our ultimate goal is to create a robust system for early detection and classification, as well as tracking, of small-size nodules before they turn into cancerous. The entire development in the chapter is model-based and data-driven, allowing design, calibration and testing for the CAD system, based on archived data as well as data accrued from new patients. We provide standard development using two clinical datasets that are already available from the ELCAP and LIDC studies.

A. A. Farag
Imaging Biomarkers and Computer-Aided Diagnosis Laboratory,
NIH, Bethesda, MD, USA

M. Farag, J. Graham, S. Elshazly and A. Farag (✉)
Department of Electrical and Computer Engineering, University of Louisville,
Louisville, KY, USA
e-mail: aly.farag@louisville.edu
url: http://www.cvip.uofl.edu

S. Elshazly
Kentucky Imaging Technologies, LLC, Louisville, KY, USA

M. al Mogy
Al Mogy Scan Center, Mansoura, Egypt

S. Li and J. M. R. S. Tavares (eds.), *Shape Analysis in Medical Image Analysis*,
Lecture Notes in Computational Vision and Biomechanics 14,
DOI: 10.1007/978-3-319-03813-1_8,

1 Introduction

In this chapter, we highlight a state-of-the-art analytic approach to lung nodule analysis using low dose CT (LDCT) of the human chest. Our focus is on small-size nodules ($\leq$1 cm in diameter) that appear randomly in the lung tissue. Radiologists diagnose these nodules by visible inspection of the LDCT scan. Despite the wide range of nodule classifications among radiologists, the nodule classification of Kostis et al. [1] is found to be particularly useful in the algorithmic evaluation presented in this work. Nodules in Kostis's work are grouped into four categories:(i) well-circumscribed where the nodule is located centrally in the lung without being connected to vasculature; (ii) vascularized where the nodule has significant connection(s) to the neighboring vessels while located centrally in the lung; (iii) pleural tail where the nodule is near the pleural surface, connected by a thin structure; and (iv) juxta-pleural where a significant portion of the nodule is connected to the pleural surface.

Figure 1 shows examples of small size nodules ($\leq$1 cm in diameter) from the four categories. The upper and lower rows show zoomed images of these nodules. Notice the ambiguities associated with shape definition, location in the lung tissues, and lack of crisp discriminatory features.

Modeling aims at representing the objects with mathematical formulation that captures their characteristics such as shape, texture and other salient features. The histogram of the object's image provides some information about its texture—the modes of the histogram indicate the complexity of the texture of the object. Figure 2 shows sample of nodules and their histograms. These histograms are essentially bimodal, for the nodule and background regions, and may be sharpened if the region of interest (ROI) is limited to be around the spatial support of the nodules.

Another difficulty of small-size nodules lies with inabilities of exact boundary definition. For example, radiologists may differ in outlining the lung nodules spatial support as shown in Fig. 3. Difference in manual annotation is common of small objects that have not well-defined description. This adds another dimension of difficulty for automatic approaches, as they are supposed to provide outputs that mimic human experts. In other words, human experts differ among themselves, how would they judge a computer output? Validation of automatic approaches for lung nodule detection, segmentation and classification - using only the visible information in an image - is an order of magnitude more difficult than that of automatic face recognition, for example.

Farag [2] studied the behavior of the intensity versus the radial distance of the nodule centroids [2]. The intensity versus radial distance distribution for small nodules was shown to decay almost exponentially. An empirical measure of the region of support of the nodules was derived based on this distribution. This approach has been tested further on three additional clinical studies in this work and has shown to hold true. The summation of the intensities of Hounsfield Units (HU) in concentric circles (or ellipses) beginning from the centroid of the nodule, decays in a nearly exponential manner with the distance from the centroid.

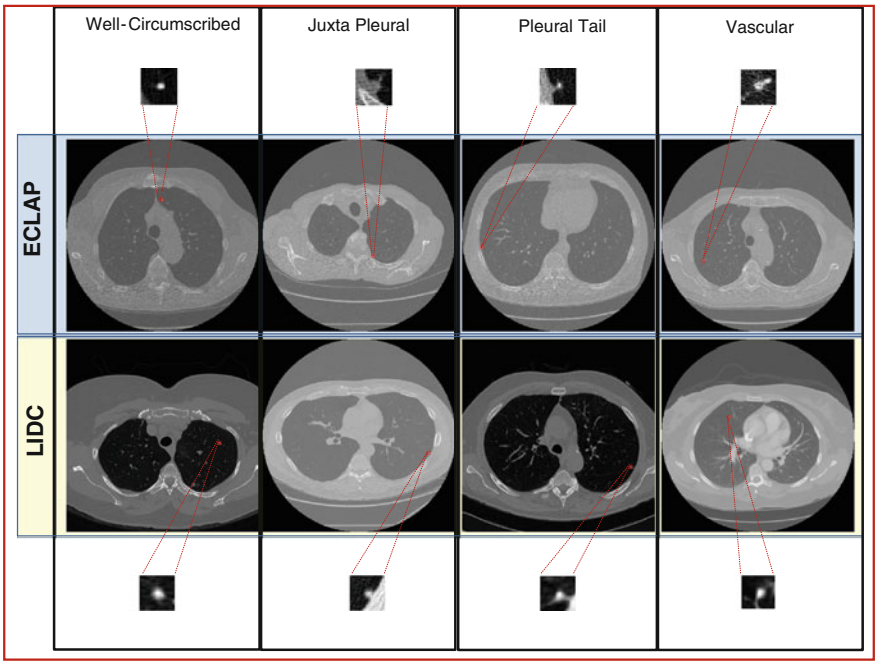

Fig. 1 Examples of lung nodules of size below 10 mm from two clinical studies. The *upper* and *lower rows* show zoomed pictures of the nodules

Figure 4 shows the radial distances for four nodule types from the LIDC clinical studies [4]. This behavior provided a clue for empirically deciding the spatial support (ROI) of the nodules—which is used for auto cropping of the detected nodules. Of course a refinement step is needed to precisely define the exact ROI of the nodule—this is carried out in nodule segmentation. This behavior is similar with the ELCAP study as well.

Object segmentation is a traditional task in image analysis. Real world objects are hard to model precisely; hence the segmentation process is never an easy task. It is more difficult with the lung nodules due to the size constraints.

Figure 5 shows the average intensity (HU) histograms of the manually cropped nodules in the ELCAP and LIDC screening studies. The histograms are distinctly bimodal and a binary classifier (thresholding) may be used for separating the nodules and non-nodules regions. The decision boundary (threshold) may be selected by various techniques, including fitting one-dimensional Gaussian density for the nodule and non-nodule regions and using the expectation-maximization approach (EM) to estimate the parameters (e.g., [2]). Unfortunately, this approach does not work well due to the uncertainties associated with the physical nodules as previously described.

There is a vast literature on object modeling and considerably larger literature on the subsequent steps of modeling; e.g., synthesis, enhancements, detection, segmen-

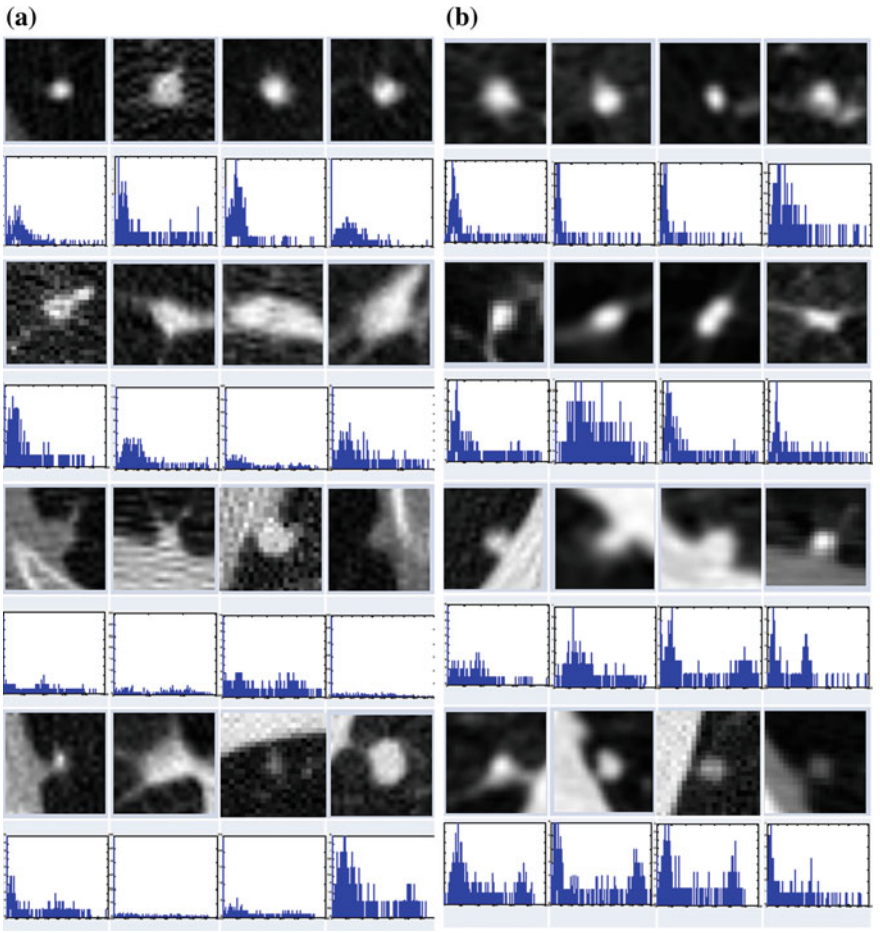

Fig. 2 Sample of nodules and their gray level (Hounsfield Units) histograms. Nodules in left are from ELCAP [3] study and those in the right table from LIDC [4] study. On *top row*, from *left* to *right*: well-circumscribed, vascular, juxta-pleural and pleural-tail nodules, respectively. **a** Nodules and histograms from the ELCAP study. **b** Nodules and histograms from the LIDC study

tation, recognition, and categorization. Farag [2] considered a five-step system for modeling of small lung nodules: (i) Acquisition and Enhancement; (ii) Parametric Modeling; (iii) Detection; (iv) Segmentation; and (v) Categorization (Classification) [2]. By constructing a front-end system of image analysis (CAD system) for lung nodule screening, all of these steps must be considered. Activities in the past few years have led to the following discoveries: (1) Feature definitions on small size objects are hard to pin point, and correspondences, among populations, is very tough to obtain automatically; (2) Classical approaches for image segmentation based on statistical maximum a posteriori (MAP) estimation and the variational level sets

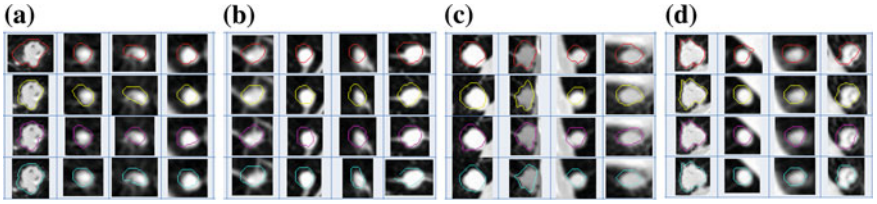

Fig. 3 Manual annotation of the main portion of the spatial support of lung nodules by *four* radiologists. Note the difference in size and shape of the annotations. **a** Outlines of fouur well-circumscribed nodules. **b** Outlines of four vascular nodules. **c** Outlines of four juxta-pleural nodules **d** Outlines of four pleural-tail nodules

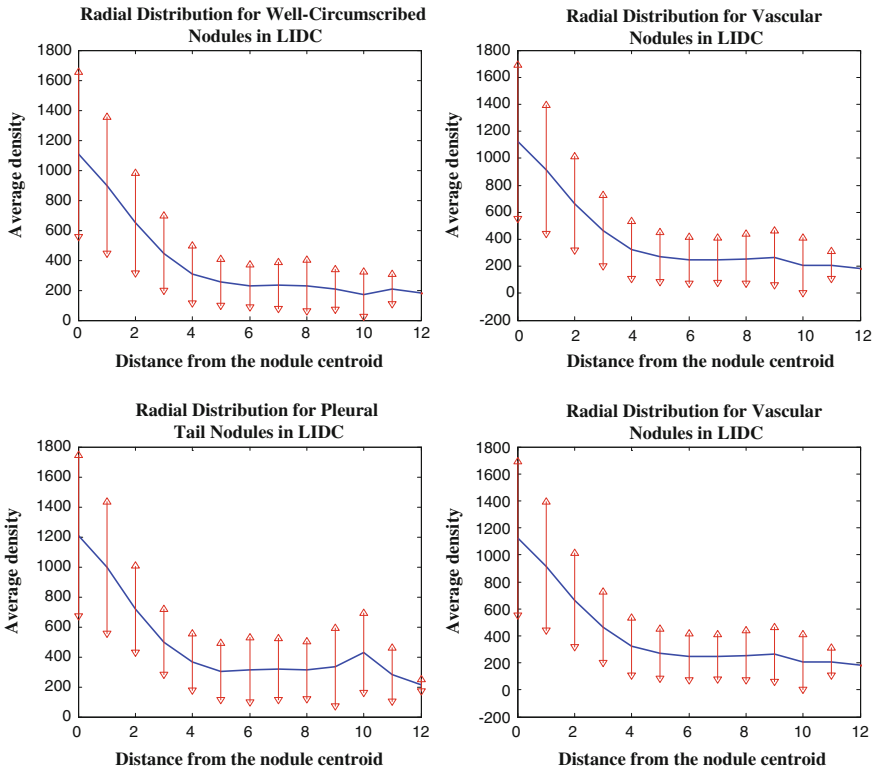

Fig. 4 Distribution of the nodule intensity (HU) for four nodule types manually cropped from the LIDC (over 2000 nodules). For nodules less than 10 mm in diameter, an ROI of size 21×21 pixels may be used

approaches do not perform well on small size objects due to unspecific object characteristics; (3) Prior information is essential to guide the segmentation and object detection algorithms—the more inclusive the a-priori knowledge, the better the performance of the automated algorithms; (4) An integration of attributes is essential for

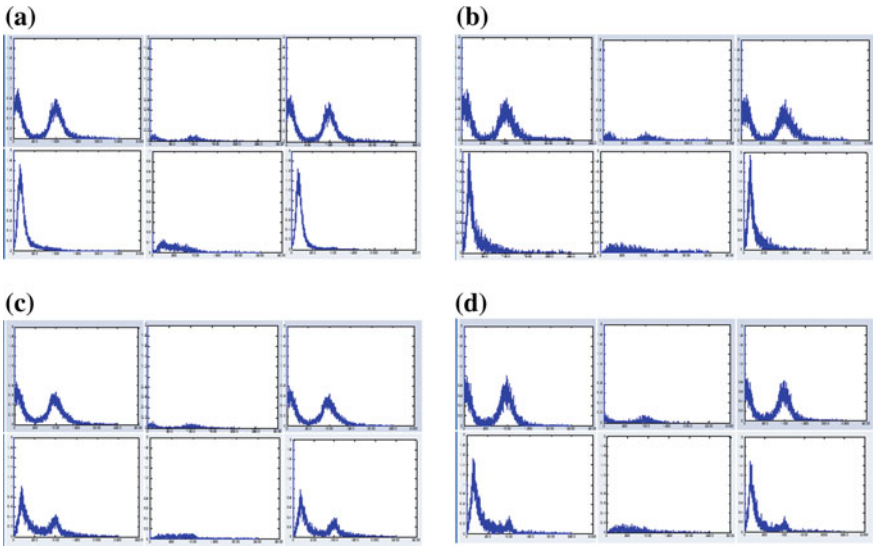

Fig. 5 The intensity (HU) histograms of the manually cropped nodules from the ELCAP and LIDC screening studies. These histograms are bio-modal showing the nodule and non-nodule regions in the ROI. These histograms are used as estimates of the probability density functions in the nodule segmentation process. **a** Intensity of well-circumscribed nodules for ELCAP (*upper*) and LIDC (*lower*) **b** Intensity of vascular nodules for ELCAP (*upper*) and LIDC (*lower*) **c** Intensity of juxta-pleural nodules for ELCAP (*upper*) and LIDC (*lower*) **d** Intensity of pleural-tail nodules for ELCAP (*upper*) and LIDC (*lower*)

robust algorithmic performance; in particular shape, texture, and approximate size of desired objects are needed for proper definition of the energy functions outlining the MAP or the level sets approaches. These factors play a major motivational role of this work.

The rest of the material in this chapter will focus on four steps related to an analytic system for lung nodule analysis: lung nodule modeling by active appearance; lung nodule detection; lung nodule segmentation; and lung nodule categorization.

2 Modeling of Lung Nodules by Deformable Models

Deformable models are common in image modeling and analysis. Random objects provide major challenges as shapes and appearances are hard to quantify; hence, formulation of deformable models are much harder to construct and validate. In this work, we devise an approach for annotation, which lends a standard mechanism for building traditional active appearance (AAM), active shape (ASM) and active tensor models (ATM). We illustrate the effectiveness of AAM for nodule detection.

Automatic approaches for image analysis require precise quantification of object attributes such as shape and texture. These concepts have precise definitions, but their descriptors vary so much from one application to another. A shape is defined to be the information attributed to an object that is invariant to scale, origin and orientation [5]. A texture may be defined as the prevalence pattern of the interior of an object [6]. Geometric descriptors identify "features" that are "unique" about an object. Shape, texture and geometric descriptors are major concepts in this work; they will be defined and used in the context of modeling small size objects under uncertainties [7]. The theoretical development in this work falls under the modern approaches of shape and appearance modeling. These models assume the availability of an ensemble of objects annotated by experts—the ensemble includes variations in the imaging conditions and objects attributes to enable building a meaningful statistical database.

Active shape models (ASM) and active appearance models (AAM) have been powerful tools of statistical analysis of objects (e.g., [8, 9]). This section highlights some of the authors' work on *data-driven* lung nodule modeling and analysis (e.g., [10, 11]), with focus on active appearance models (AAM).

2.1 Lung Nodule Modeling

Real world objects may take various forms of details, and may be linear, planar or three-dimensional. In [7], Dryden and Marida, define *anatomical landmarks* as points assigned by an expert that corresponds between organisms in some biologically meaningful way; *mathematical landmarks* as points located on an object according to some mathematical or geometrical property, i.e. high curvature or an extremum point; and *pseudo-landmarks* as constructed points on an object either on the outline or between landmarks. Figure 6 is a sample of small-size nodules smaller than 1 cm in diameter from the LIDC [4] clinical study, showing the variations that can be captured by shape and appearance models.

From a computer vision prospective, AAM and ASM modeling have been used with great successes in objects having distinct landmarks (e.g., [8, 9]). A shape is considered to be a set of $n-$vertices $x \in R^k$; for the two-dimensional case:

$$\boldsymbol{x} = [x_1; x_2; \cdots; x_n; y_1; y_2; \cdots; y_n]^T \tag{1}$$

The shape ensemble (realizations of the *shape process* of a certain object) is to be adjusted (aligned) on the same reference to enable filtering of scale, orientation and translation among the ensemble, per the shape definition. This alignment generates the so-called *shape space*, which is the set of all possible shapes of the object in question. To align the shapes in an ensemble, various procedures may be used. The *Procrustes* procedure is common for *rigid* shape alignments. The alignment process removes the redundancies of *scale*, *translation* and *rotation* using a similarity measure that provides the minimum *Procrustes distance*.

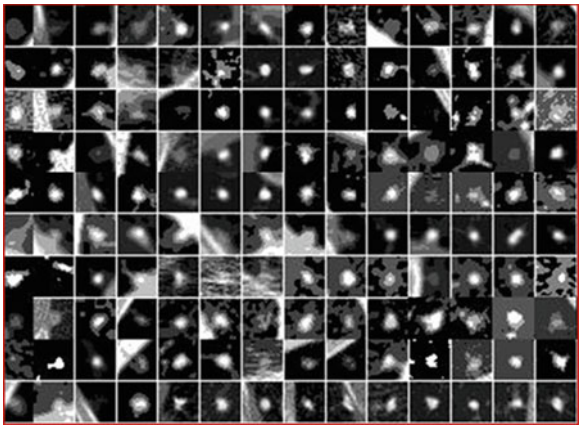

Fig. 6 An ensemble of 140 nodules manually cropped from the LIDC study

Suppose an ensemble of shapes is available with one-to-one point (feature) correspondence is provided. The Procrustes distance between two shapes s_1 and s_2 is the sum of squared distance (SSD)

$$P_d^2 = \sum_{j=1}^{n} \left(x_{j_1} - x_{j_2}\right)^2 + (y_{j_1} - y_{j_2})^2 \tag{2}$$

Annotated data of an ensemble of shapes of a certain object carries redundancies due to imprecise definitions of landmarks and due to errors in the annotations. Principal Component Analysis (PCA) may *be used for reducing these* redundancies. In PCA, the original shape vector is linearly transformed by a mapping such that has $\mathbf{z} = \mathbf{M}\mathbf{x}$ less correlated and highly separable features. The mapping $\mathbf{M}$ is derived for an ensemble of N shapes as follows**:**

$$\bar{x} = \frac{1}{N}\sum_{i=1}^{N} x_i;\ \sum_x = \frac{1}{N}\sum_{i=1}^{N} (x_i - \bar{x})(x_i - \bar{x})^T \tag{3}$$

are the mean and covariance of $\mathbf{X}$. Therefore, the mean and covariance of $\mathbf{z}$ would be**:**

$$\bar{z} = \frac{1}{N}\Sigma_{j=1}^{N}\mathbf{z}_j \tag{4a}$$

$$\Sigma_{\mathbf{z}} = \frac{1}{N}\Sigma_{i=1}^{N}(\mathbf{z}_i - \bar{z})(\mathbf{z}_i - \bar{z})^T = \mathbf{M}\Sigma_x\mathbf{M}^T \tag{4b}$$

If the linear transformation $\mathbf{M}$ is chosen to be orthogonal; i.e., $\mathbf{M}^{-1} = \mathbf{M}^T$, and selecting it as the eigenvectors of the symmetric matrix $\sum_x$, this would make $\sum_z$ to be a diagonal matrix of the eigenvalues of $\sum_x$. The eigenvectors corresponding to the small eigenvalues can be eliminated, which provides the desired reduction.

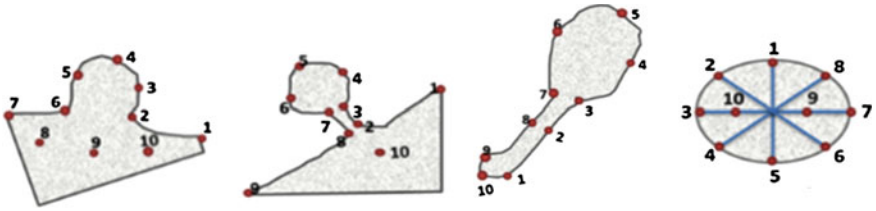

Fig. 7 Definition of Control points (landmarks) for nodules. *Right*-to- *left*: juxta-pleural, pleural tail, vascular, a well-circumscribed nodule models

Therefore , $\mathbf{x}$ may be expressed as:

$$\mathbf{x} = \bar{\mathbf{x}} + \mathbf{P}\,\mathbf{b} \tag{5}$$

where $\mathbf{P} = (\boldsymbol{p}_1|\boldsymbol{p}_2|\ldots|\boldsymbol{p}_m)$ matrix of m largest eigen vectors of $\sum_x$ and $\mathbf{b} = \mathbf{P}^{\mathbf{T}}(\mathbf{x} - \bar{\mathbf{x}})$ **is an** $m \times 1$ vector. Equation (5) is the statistical shape model, which is derived using PCA. By varying the elements of $\mathbf{b}$ one can vary the synthesized shape $\mathbf{x}$ in Eq. (5). The variance of the ith parameter $b_i \in \mathbf{b}$ can be shown across the training set to be equal to the eigenvalue λ_i [8].

2.2 Nodule Annotation

In order to construct the active appearance or active tensor models, we need an annotated ensemble of objects. In case of random objects, the annotation process becomes extremely difficult; it takes yet another level of difficulty with small-size. Yet, the major goal of this work is to address such objects, specifically, small size lung nodules, which are used for early detection screening of possible lung cancer. We used the fuzzy description of lung nodules from Kostis et al. [1] to devise a feature definition approach for four categories of nodules; *well-circumscribed*, *vascularized, juxta-pleural* and *pleural-tail* nodules. Figure 7 illustrates the landmarks that correspond to the clinical definition of these four nodule categories.

Using the above definitions, we created a manual approach to annotate the nodules. First, we take the experts' annotation, zoom it and manually register it to a template defining the nodule type/category, and then we select the control points on the actual nodule using the help of the template. This annotation enabled creation of active appearance models, which mimics largely the physical characteristics of lung nodules that cannot be modeled otherwise.

Figure 8 shows examples for the nodule models generated by ensembles from the ELCAP and LIDC clinical lung screening studies**.** The average nodules (shown in Fig. 8) capture the main features of real nodules. Incorporation of other basis has been studied in Farag et al. [11]. Figure 9 shows examples of AAM nodule models with additional "Eigen nodules".

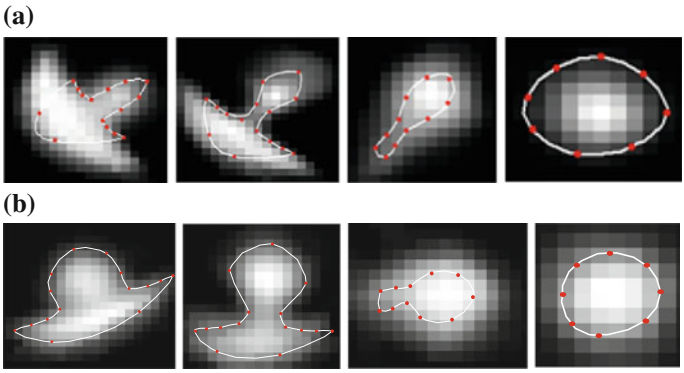

Fig. 8 AAM Models for lung nodules from clinical CT scans. *Right*-to-*left*: juxta-pleural, pleural tail, vascular, a well-circumscribed nodule models. **a** Average nodules from ELCAP study. **b** Average nodules from LIDC study

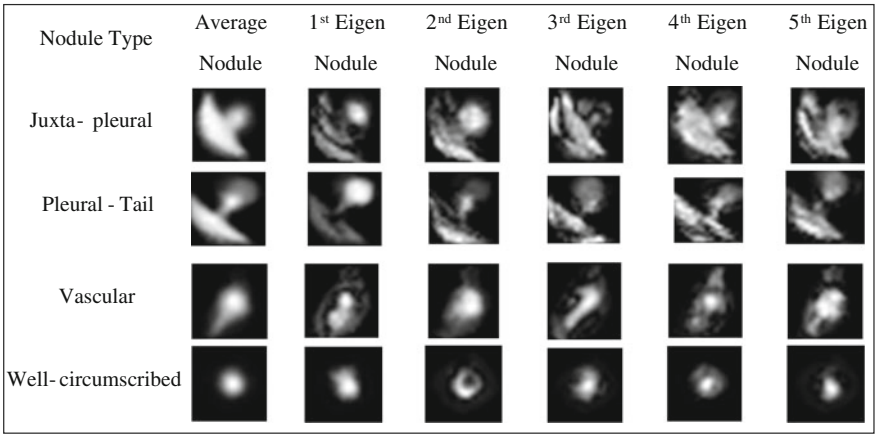

Fig. 9 Average and 1st five eigen nodules on ELCAP study

3 Lung Nodule Detection

The above modeling approach has provided tremendous promise in three subsequent steps of lung nodule analysis: detection, segmentation, and categorization. Due to space limitations, we only consider lung nodule detection using the AAM nodule models. Further, we use only a basic detection approach that is based on template matching with normalized cross-correlation (NCC) as similarity measure. Other measures have been examined in our related work (e.g., [11]). We report the detection performance by constructing the ROC of both the ELCAP and LIDC clinical studies. We chose to limit the ensemble size for modeling to be 24 *per nodule type* for the two studies, to provide a comparison with our earlier work [10]. The ROCs are

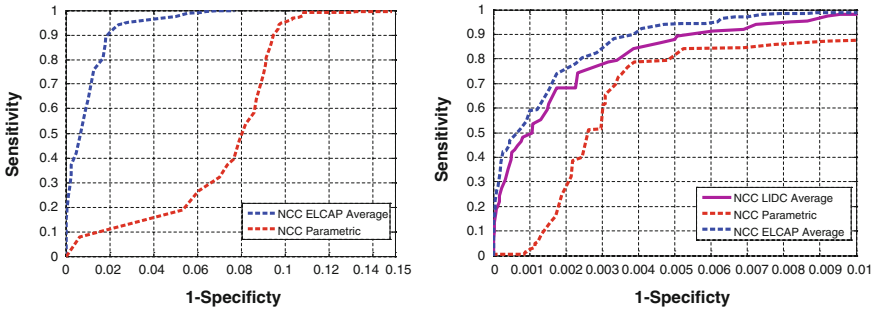

Fig. 10 ROC curves for template matching detection on the ELCAP and LIDC database versus the circular and semi-circular models. **a** ROC for the ELCAP study. **b** ROC for the LIDC study

built to show the overall *sensitivity* and of the detection process. The textures of the parametric nodules were generated by the analytical formulation in our earlier work (e.g., [10]).

3.1 Clinical Evaluation

ELCAP Data: The ELCAP database [3] contains 397 nodules, 291 identified and categorized nodules are used in the detection process. Results using only the average (mean) template models generated from the AAM approach is examined against parametric nodule models, (i.e. circular and semi-circular) of radius 10, templates in this first set of experiments.
LIDC Data: The Lung Imaging Data Consortium (LIDC) [4] contains 1018 helical thoracic CT scans from 1010 different patients. We used ensembles of 24 nodules per nodule type to design the nodule models (templates) and the rest to test the detection performance.

Figure 10 shows the ROC of 1—specificity versus sensitivity. The results show the superior performance of the AAM-models over the parametric models. In generating these ROC curves, we used the mean in the AAM models as the nodule template (note: in [11] we used other *eigen-nodules* besides the mean).

We note from Figure 10 that the templates from the ELCAP ensemble provided better performance than those from the LIDC ensemble. This because the wide range of variations in texture information found in the LIDC database, which affects the appearance of the resulting nodule model (template). We used 24 nodules, per nodule type, in both ELCAP and LIDC in order to have even comparison. It is expected that the better AAM models result with larger ensemble size; which is possible with the LIDC study as it contains over 2000 nodules vs. ELCAP which is only few hundreds.

3.2 Extensions

We note that in the ELCAP database, the data acquisition protocol was the same throughout; very low resolution. That was reflected in the AAM model, showing a texture that is relatively more homogenous than that in the LIDC case, which uses data from various imaging centers and various imaging scanners, with somewhat variable range of Hounsfield Units (HU). In general, if we include more nodules in the design, we expect a better appearance modeling; the LIDC database allows such choice.

This section dealt with modeling of small-size lung nodules using two clinical studies, the ELCAP and LIDC. We discussed the process of nodule annotation and the steps to create AAM nodule models. These models resemble the real nodules, thus using them as templates for nodule detection is more logical than the non-realistic parametric models. These types of models add two additional distinctions over the parametric approaches; it can automate the processes of nodule segmentation and categorization. Tensor modeling may also be used to generate the nodule models. From the algorithmic point of view, an *adaboost* strategy for carrying out the detection may lend speed advantage over the typical cross-correlation implementation used in this work.

4 Nodule Segmentation

This section describes a variational approach for segmentation of small-size lung nodules which may be detected in low dose CT (LDCT) scans. These nodules do not possess distinct shape or appearance characteristics; hence, their segmentation is enormously difficult, especially at small size ($\leq$1 cm). *Variational methods hold promise in these scenarios despite the difficulties in estimation of the energy function parameters and the convergence. The proposed method is analytic and has a clear implementation strategy for LDCT scans.*

The lungs are a complex organ which includes several structures, such as vessels, fissures, bronchi or pleura that can be located close to lung nodules. Also, the main "head" of the nodule is what radiologists consider when computing the size. In the case of detached nodules (i.e. well-circumscribed nodules) the whole segmented nodule is considered in size computations and growth analysis, while in detached nodules (i.e. juxta-pleural, vascularized and pleural-tail) the "head" is required to be extracted from the anatomical surrounds. Intensity-based segmentation [13, 14] has been applied to nodule segmentation using local density maximum and thresholding algorithms. These classes of algorithms are primarily effective for solitary nodules (well-circumscribed), however, fail in separating nodules from juxtaposed surrounding structures, such as the pleural wall (i.e., juxta-pleural and pleural-tail nodules) and vessels (vascular nodules), due to their similar intensities.

More sophisticated approaches have been proposed to incorporate nodule-specific geometrical and morphological constraints (e.g., [1, 15–17]). However, juxta-pleural, or wall-attached, nodules still remain a challenge because they can violate geometrical assumptions and appear frequently. Robust segmentation of the juxta-pleural cases can be addressed in two approaches: a) global lung or rib segmentation (e.g., [18]), and b) local non-target removal or avoidance [14]. The first can be effective but also computationally complex and dependent on the accuracy of the whole-lung segmentation. The second is more efficient than the former but more difficult to achieve high performance due to the limited amount of information available for the non-target structures. Other approaches have been proposed in the literature (e.g., [19]), but require excessive user interaction. In addition, some approaches assumed predefined lung walls before segmenting the juxta-pleural nodules (e.g., [20]).

4.1 Variational Approach for Nodule Segmentation

The level set function as a signed distance map is able to capture complicated topological deformations. A level set function $\emptyset : \Omega \subset R^2 \rightarrow R$ can be defined as the minimum Euclidean distance between the point $\mathbf{X} \in \Omega$ and the shape boundary points. A curve can be initialized inside an object, and then evolves to cover the region guided by image information. The evolving curve within the level set formulation is a propagating front embedded as the zero level of a 3D scalar function $\emptyset(\boldsymbol{X}, t)$, where $\boldsymbol{X}$ represents a location in space. In order to formulate the intensity segmentation problem, it is necessary to involve the contour representation. Given an image $I : \Omega \subset R^2 \rightarrow R$, the segmentation process aims to partition the image into two regions: object (inside the contour denoted by **o**) and background (outside the contour denoted by **b**). An error term can be computed by counting the number of correctly classified pixels and then measuring the difference with respect to the total number of pixels. This can be done by summing up the probabilities of the internal pixels to be *object* and the external pixels probabilities to be classified as *background*. This is measured by the term:

$$Error = 1 - \pi_o \int_{\Omega_o} P_o(I(\boldsymbol{X}))\, d\Omega - \pi_b \int_{\Omega_b} p_b(I(\boldsymbol{X}))\, d\Omega \tag{6}$$

where p_o and p_b are the probabilities of the object and background according to the intensity values (Gaussian distributions are used to model these regions). Prior probabilities of regions (π_o and π_b) are involved in the formulation as well. Minimizing this error term is equivalent to minimizing the energy functional:

$$E(\emptyset) = -\pi_o \int_{\Omega_o} p_o H_\epsilon(\emptyset)\, d\Omega - \pi_b \int_{\Omega_b} p_b H_\epsilon(-\emptyset)\, d\Omega \tag{7}$$

where H is the Heaviside step function and $\epsilon \in R^+$ represents the narrow band region width. An extra term is added to the energy function to represent the contour arc-length (L) which also needs to be minimal to guarantee a smooth evolution. The new energy will be:

$$E(\emptyset) = -\pi_o \int_{\Omega_o} p_o H_\epsilon(\emptyset)\, d\Omega - \pi_b \int_{\Omega_b} p_b H_\epsilon(-\emptyset)\, d\Omega + \lambda L \tag{8}$$

where $\lambda \in R^+$. The level set function evolves to minimize such a functional using the Euler-Lagrange formulation with the gradient descent optimization:

$$\frac{\partial \emptyset}{\partial t} = \delta_\epsilon(\emptyset)(\pi_o p_o - \pi_b p_b) + \lambda \mathrm{k} \tag{9}$$

where δ is the derivative of the Heaviside function and k is the curvature. Thus, the evolution depends on the local geometric properties (local curvature) of the front and the external parameters related to the input data I. The function $\emptyset(\cdot\,,\cdot)$ deforms iteratively according to the above equation, while solving $\emptyset(\boldsymbol{X}, t = 0$ gives the position of the 2D front iteratively. Let $\emptyset_g$ denote the intensity segmented region function representation The Gaussian distribution and prior probabilistic parameters are computed according to the method in [21].

4.2 Shape Alignment

This process aims to compute a transformation $\mathbf{A}$ that moves a source shape (α) to its target (β). The in-homogeneous scaling matching criteria from [21] is adopted, where the source and target shapes are represented by the signed distance functions $\emptyset_\alpha$ and $\emptyset_\beta$ respectively. The transformation function is assumed to have scaling components: $\boldsymbol{S} = diag(s_x, s_y)$, rotation angle, θ (associated with a rotation matrix $\mathbf{R}$) and translations: $\boldsymbol{T} = [T_x, T_y]^T$ A dissimilarity measure to overcome the scale variance issue is formulated by assuming that the signed distance function can be expressed in terms of its projections in the coordinate directions as: $\mathbf{d}_\alpha = [d_x, d_y]^T$ at any point in the domain of the shape α . Applying a global transformation $\mathbf{A}$ on $\emptyset_\alpha$ results in a change of the distance projections to $\mathbf{d}'_\alpha = \mathbf{RSd}_\alpha$ which allows the magnitude to be defined as: $\emptyset'_\alpha = ||\mathbf{Sd}_\alpha||$ which implies that $\emptyset'_\alpha \leq \max(s_x, s_y)\emptyset$ Thus, a dissimilarity measure to compute the difference between the transformed shape and its target representation can be directly formulated as:

$$r(\mathbf{X}) = ||\mathbf{RSd}_\alpha(\mathbf{X})|| - \emptyset_\beta(\mathbf{A}). \tag{10}$$

By summing-up the squared difference between the two representations, an energy function can be formulated as:

$$E_1 = \int_{\Omega} \delta'_{\epsilon}(\emptyset_{\alpha}, \emptyset_{\beta})\, r^2\, d\Omega \tag{11}$$

where δ'_{ϵ} reduces the complexity of the problem and ϵ is the width parameter of the band around the shape contour. The given measure r, from the shown derivations, satisfy the relation $r \leq s\emptyset_{\alpha}(\mathbf{X}) - \emptyset_{\beta}(\mathbf{A})$, where $s = \max(s_x, s_y)$. Thus, an energy function can be obtained where $E \leq E_1$;

$$E = \int_{\Omega} \delta'_{\epsilon}(\emptyset_{\alpha}, \emptyset_{\beta})\, \left(s\emptyset_{\alpha}(\mathbf{X}) - \emptyset_{\beta}(\mathbf{A})\right)^2 d\Omega \tag{12}$$

The above functional better describes the registration since it incorporates a scaled version of the source shape representation. In this work, the gradient descent optimization is used to solve the problem, which requires the involved functions to be differentiable. A smeared version of $s(s_x, s_y) = \max(s_x, s_y)$, is used at the line since, $(s_x = s_y)$ the function is not differentiable there, which is based on its original definition:

$$s(s_x, s_y) = \max(s_x, s_y) = s_x H_{\epsilon}(s_x - s_y) + s_y(1 - H_{\epsilon}(s_x - s_y)) \tag{13}$$

which will return s_x if $s_x - s_y \geq 0$, otherwise s_y. The smeared Heaviside step function H is used to obtain a smooth transition around the line $s_x = s_y$ allowing the function to be differentiable everywhere. The function derivatives will be calculated as

$$\frac{\partial s}{\partial s_x} = H_{\epsilon}(s_x - s_y) + (s_x - s_y)\delta_{\epsilon}(s_x - s_y) \tag{14}$$

$$\frac{\partial s}{\partial s_y} = H_{\epsilon}(s_y - s_x) + (s_y - s_x)\delta_{\epsilon}(s_y - s_x) \tag{15}$$

The parameters $\{s_x, s_y, \theta, T_x, T_y\}$ are required to minimize the energy functional E.

4.3 Level Set Segmentation Algorithm with Shape Prior

The above steps have resulted in an algorithm whose input is LDCT scans and output is segmented lung nodules. The algorithm can be summarized as follows:

***Lung Nodule Segmentation Algorithm*:**

1. Segment the Lungs from their surroundings—*Lung tissue segmentation* (e.g., [22]).
2. Train the lung nodule modeling step on a portion of the data at hand—*Lung Nodule Modeling*
3. Apply the lung nodule detection approach to compute the positions of the candidate nodules and hence crop them for classification. Cropping here means setting a

box around the nodule center and extracts its neighbor area from the surroundings; i.e., a region of interest, ROI, is cropped around the detected nodules—*Nodule detection and ROI determination*
4. Based on the input image size, construct the initial prior shape circle and its shape model representation $\emptyset_p$.
5. Solve Eq. 8 to compute the intensity segmentation region representation $\emptyset_g$. Solution is iterative until the function converges—reaches a certain state. Note the function keeps the sign distance property by following the approach in [22].
6. Initialize the transformation parameters to $s_x = 1, s_y = 1$ and . $\theta = 0$ At this moment the nodule center location is manually selected which initializes the translation parameters t_x and ty
7. Solve the gradient descent approach to minimize the energy in Eq. 11. Parameters converge to their steady state values and hence the final boundaries of the ellipse are computed.
8. Threshold the region inside the ellipse to accurately mark the nodule pixels. The resulting region may undergo a median filter smoothing step to remove noisy pixels.

4.4 Some Results

This work is validated using four different databases. The first is the ELCAP [3] public database, DB1.This database has nodules of diameter ranging from 2 to 5 mm. The second database (DB2) contains 108 nodules from LDCT scans of slice thickness 2.5 mm and a pixel-spacing of 0.72461×0.72461 mm (diameter from 2.9 to 6 mm). The third database (DB3) has 28 nodules, 1.25 and 2.5 mm slice thickness, and nodules diameter ranging from 7 to 20 mm. The fourth dataset is the LIDC (DB4) which contains nodules ranging in sizes. The slices are both low-dose and high-dose CT images [4].

Figure 11 demonstrates the performance of a number of model-based methods for nodule segmentation. Nodules are cropped by four different radiologists, and the approaches are applied to these cropped nodules. Overall the variational shape-based level set method provided the best segmentation results for obtaining the "head" of the nodule region. The results show that the intensity-based approaches can be used as an initial or post segmentation process to the variational shaped-based level sets. Also, approaches where a shape model can be embedded into the formulation of the segmentation method are necessary for such cases as nodule segmentation.

The developed approach uses a region of interest (ROI) image that contains the lung nodule as input. Image intensity segmentation using level sets (as described above) is used to extract the non-lung regions from the lung tissue regions and represents the slices by a level set function ($\emptyset_g$). Different scales, rotation, and translation parameters are computed in each case to obtain an ellipse exactly around the nodule head (see Fig. 12). Changes of the shape model can be noticed until the

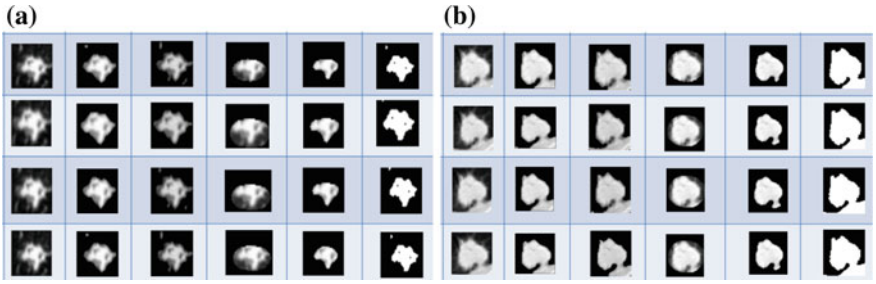

Fig. 11 Nodule segmentation by a number of approaches. Columns 5 and 6 show results of the variational approach with and without shape alignments. First column is a nodule segmented by four radiologists. Second column is the EM segmentation. Third column is the level set method. Fourth column is level sets plus shape priors. Fifth column is EM plus shape priors. Last column is graph cuts. **a** Nodule centrally located in the lung tissue. **b** Nodules connected to the pleural surface

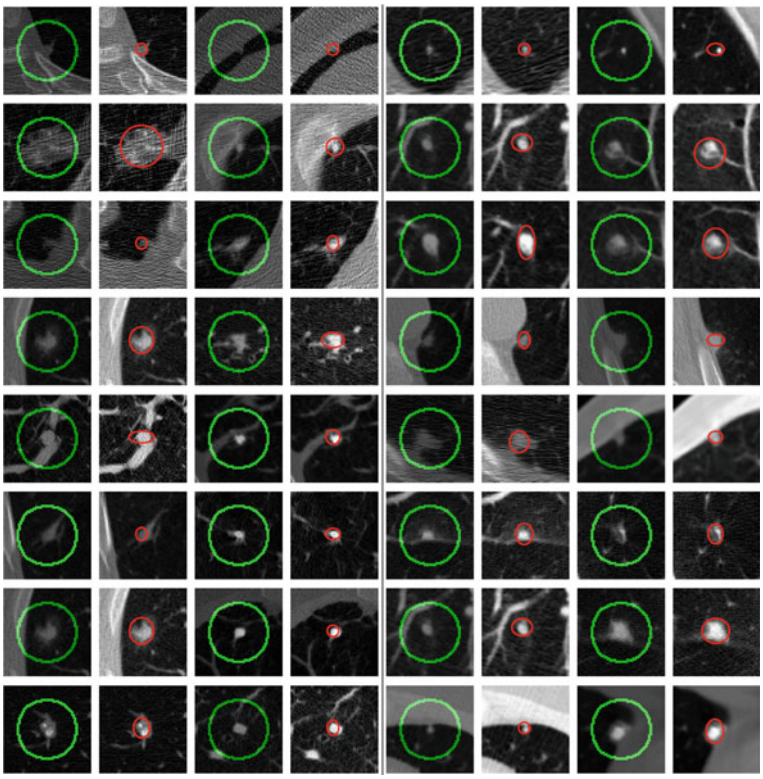

Fig. 12 Nodule segmentation results from DB1 (*left* block-first four columns) and DB2 (*right* block-last four columns). Initialization is given in green while final nodule boundaries are shown in *red*

steady state around the nodule boundaries is reached. Also, the axis of the ellipse rotates and varies in size to include the most boundary information of the nodule. The approach is robust for various nodule sizes from larger nodules (<1 cm) to nodules that occupy smaller spatial support regions (i.e. >1 cm). Similar results are obtained from other databases (e.g., [12, 23]).

4.5 Extensions

Among the possible extensions of the above algorithm are the following:

a. Proper modeling of the shape shape priors in the statistical segmentation approach.
b. Generlizing the transformation paramters that embed the shape model into the image domain, thus, avoiding the post EM step;
c. Incorporatation of the shape priors into the energy function, of general topological cliques in the MGRF models, and evaluation of the segmentation algorithm with respect to variational shape-based techniques such as level sets.

The nodule segmentation is a componenet of the CAD system for analysis of lung nodules; it requires exhaustive validation by large scale clinical studies and various radiologists.

5 Nodule Categorization

In the computer vision and biomedical imaging literature the terms categorization, classification, identification, and recognition share a lot of commonality of methods and purpose. In the lung nodule example, one may also denote the classification step as recognition. However, classification may indeed entail two aspects: assigning segmented objects into types (classes, such as the four nodule types that we have been considering in this chapter), or assigning them into a definitive group (e.g., pathology in the lung nodule case). Our focus is on descriptors that adhere to shape and appearance contexts

5.1 Object Feature Descriptors

In the past decade, several object descriptors have been introduced in the computer vision literature, including the local binary pattern (LBP) [24] and the scale-invariant feature transform (SIFT) [25]. A comprehensive evaluation of the geometric feature descriptors may be found elsewhere, in particular Mikolajczyk and Schmid 2005 [26]. Below we describe the LBP and SIFT descriptors and their performance for small-size nodule categorization (see [23] for detailed evaluation).

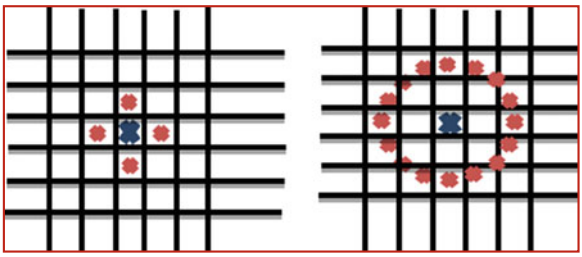

Fig. 13 Circularly symmetric neighbor sets for different values of (P , R); *left* (a) P = 4, R = 1.0; *right* P = 16, R = 2.0

5.1.1 Multi-Resolution Local Binary Pattern (LBP)

The Local Binary Pattern is an operator invariant to monotonic changes in grayscale and can resist illumination variations as long as the absolute gray-level value differences are not badly affected (e.g., [24]). The original operator labeled the pixels of an image by thresholding the 3×3 neighborhood of each pixel with the center value and considered the result as a binary number. At a given pixel position (x_c, y_c), the decimal form of the resulting 8-bit word is

$$\mathrm{LBP}(\mathrm{x_c}, \mathrm{y_c}) = \sum_{\mathrm{i}=0}^{7} \mathrm{s}(\mathrm{I_i} - \mathrm{I_c})2^{\mathrm{i}} \tag{16}$$

where, $\mathrm{I_c}$ corresponds to the center pixel $(\mathrm{x_c}, \mathrm{y_c})$, $\mathrm{I_i}$ to gray level values of the *eight* surrounding pixels and function $\mathrm{s}(\cdot)$ is a unit-step function.

The LBP operator was extended to a circular neighborhood of different radius size to overcome the limitation of the small original 3×3 neighborhood size failing to capture large-scale structures. Each instance is denoted as (P, R), where P refers to the equally spaced pixels on a circle of radius R. The parameter P controls the quantization of the angular space and R determines the spatial resolution of the operator. An LBP pattern is considered uniform if it contains at most two bitwise transitions from 0 to 1 and vice-versa, when the binary string is circular. The reason for using uniform patterns is that they contain most of the texture information and mainly represent texture primitives. The operator is derived on a circularly symmetric neighbor set of P members on a circle of radius R denoting the operator as LBP^{u2}_{PR}.

Figure 13 illustrates examples of circularly symmetric neighbor sets for various (P, R). The LBP operator was further enhanced by combining it with a rotation invariant measure $VAR_{P,R}$, which characterizes the contrast of local image texture. The combination of the LBP^{u2}_{PR} operator and the variance measure produces a powerful operator that is rotation and gray-scale invariant.

In the multi-resolution analysis the responses of multiple operators realized with different (P , R) are combined together and an aggregate dissimilarity is defined as the sum of individual log-likelihoods computed from the responses of individual operators [24]. The notation LBP^{u2}_{PR} used in this chapter refers to the extended LBP

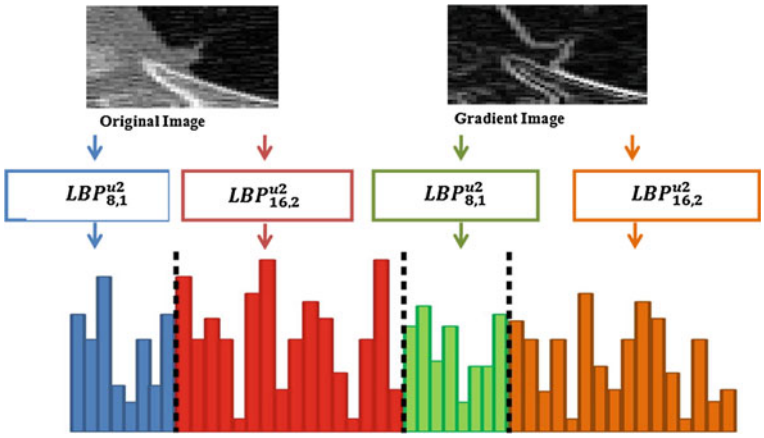

Fig. 14 Block diagram of generating the LBP for a juxta-pleural nodule. The equation for the above picture is: $\mathbf{LBP}^{u2}_{8,1} + \mathbf{LBP}^{u2}_{16,2} + \mathbf{LBP}^{u2}_{8,1} + \mathbf{LBP}^{u2}_{16,2}$, where the first two terms represent the original image and the last two terms represent the gradient image

operator in a neighborhood, with only uniform patterns considered. The LBP is used to generate a feature vector which describes the nodule region of interest in a LCDT slice. The LBP is applied to one of three scenarios on: (i) the original nodule images; (ii) the gradient of the nodule image or, (iii) an addition of the original and gradient nodule images. The gradient image was computed by first obtaining each individual image in the x- and y-spaces by filtering the corresponding directional-space original image with the corresponding parameter vector identified in the author's work (e.g., [23, 27]); the overall gradient nodule image is:

$$\nabla_{\text{nodule}} = \sqrt{\nabla_{\text{x}}^2 + \nabla_{\text{y}}^2} \tag{17}$$

A similarity measure is then used to classify these nodules to one of the four classes: juxta, well-circumscribed, pleural tail and vascularized. Principle component analysis (PCA) and linear discriminant analysis (LDA) are used to project the extracted LBP descriptors to a low-dimensional subspace where noise is filtered out. Figure 14 illustrates the formation of the LBP descriptors on lung nodules.

5.1.2 The Signed Distance Transform

The distance transform is a shape-based feature descriptor that represents each pixel of the binary edge map image with a distance to the nearest obstacle pixel (i.e., binary pixel). The extracted Signed Distance transform images were projected to a lower-dimensional subspace using PCA and LDA. The LBP of the signed distance image results were also obtained, thus, resulting in a combinational shape and texture feature descriptor representation of the nodules and non-nodules. The relevance of

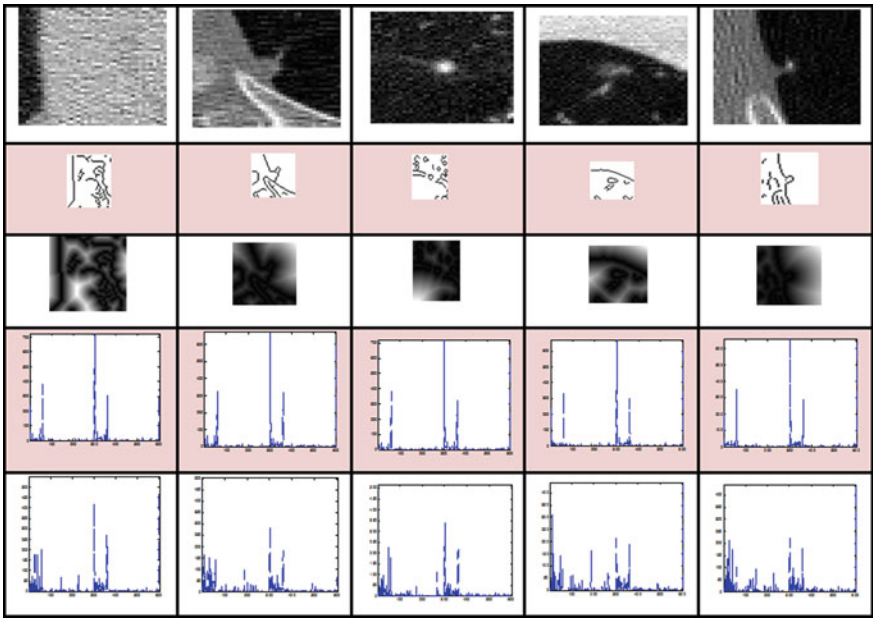

Fig. 15 *First* row shows typical non-nodule (*first*column) and nodule textures (juxta-pleural, well-circumscribed, vascularized and pleural tail, respectively). *Second* row shows edge maps (using the Canny Operator). *Third* row is the signed distance. *Fourth* row is the LBP of the nodules. Final results depict the LBP + Signed distance features

combining shape and texture feature vectors is described in the recognition stage. Figure 15 illustrates the approach which combines the LBP and Signed Distance Transform.

5.1.3 The Scale-Invariant Feature Transform (SIFT)

The SIFT is a combinational detector and descriptor approach introduced by Lowe [25] that allows extraction of distinctive scale and rotation invariant features from images. The SIFT is a combination of a scale invariant region detector known as the difference of Gaussian (DoG) detector and a proper descriptor referred to as SIFT-key. The approach consists of four major steps of computation to generate the set of image features: Scale Space extrema detection, Key-point Localization, Orientation assignment and Key-point descriptor. In the first stage of computation all scales and image locations are searched over using a DoG function to identify potential interest points that are invariant to orientation and scale. Once the potential interest points are found at each candidate location a detailed model is fitted to determine scale and location.

The keypoints selected are based on the stability measures. To each keypoint location one or more orientations are assigned based on the local image gradient directions. All future operations are performed on image data that has been transformed relative to the assigned scale, location and orientation for each feature. At the selected scale in the region around each keypoint the local image gradients are measured and transformed into a representation that allows for significant levels of change illumination and local shape distortion. The scale-space of an image defined as a function, $L(x, y, \sigma)$, was shown by Koenderink [28] and Lindeberg [29] as follows: The only possible scale-space kernel, under reasonable assumptions, is the Gaussian function, thus the scale-space of an image $L(x, y, \sigma)$ is produced from convolving a variable-scale Gaussian, $G(x, y, \sigma)$, with an input image, $I(x, y)$:

$$L(x, y, \sigma) = G(x, y, \sigma) * I(x, y) \tag{18}$$

Lowe proposed using scale-space extrema in the difference-of-Gaussian function, to accurately detect stable keypoint locations in scale-space, convolved with the image, $D(x, y, \sigma)$ which from the difference of two nearby scales separated by a constant multiplicative k factor can be computed:

$$D(x, y, \sigma) = (G(x, y, k\sigma) - G(x, y, \sigma)) * I(x, y) = L(x, y, k\sigma) - L(x, y, \sigma) \tag{19}$$

In order to detect the local maxima and minima of $D(x, y, \sigma)$, each sample point is compared to its eight neighbors in the current image and nine neighbors in the scale above and below. The keypoint is selected if it larger or smaller than all of these neighbors. Once the keypoint candidate is obtained a detailed fit to the nearby data for location, ratio of principal curvatures and scale is performed to reject points with low contrast or poorly localized along an edge. Consistent orientation assignment to each keypoint based on local image properties allows the keypoint descriptor to be represented relative to this orientation and thus achieve invariance to image rotation. The scale of the keypoint is used to select the Gaussian smoothed image, L, with the closest scale. Each image sample, $L(x, y)$, at this scale, the gradient magnitude, $m(x, y)$ and orientation $\theta(x, y)$ is pre-computed using pixel differences:

$$m(x, y) = \sqrt{(L(x+1, y) - L(x-1, y))^2 + (L(x, y+1) - L(x, y-1))^2} \tag{20}$$

$$\theta(x, y) = \tan^{-1}(L(x, y+1) - L(x, y-1) / (L(x+1, y) - L(x-1, y))) \tag{21}$$

An orientation histogram of 36 bins covering the 360° range of orientations is formed from the gradient orientation of sample points within a region around the keypoint. Additional samples added to the histogram is weighted by its gradient magnitude and by a Gaussian-weighted circular window with a σ that is 1.5 times that of the scale of the keypoint. All the weighted gradients for the descriptor are normalized to the main orientation of the circular region around the keypoint which is divided into 4×4 non-overlapping patches. The histogram gradient orientations

within the patches are computed and then histogram smoothing is performed to avoid sudden orientation changes and bin size reduction to eight bins to limit the descriptor's size results into a $4 \times 4 \times 8 = 128$ dimensional feature vector for each key-point. The feature vector is finally normalized to unit length and thresholded to reduce the effects of linear and non-linear illumination changes.

In nodule analysis framework, it is assumed that nodules have been already detected which correspond to interest/key points in Lowe's algorithm; hence, this step can be bypassed. In order to obtain a nodule SIFT descriptor which is invariant to orientation, a consistent orientation should be assigned to the detected nodule which is represented by its centroid, x_o. This orientation is based on the gradient of the nodule's local image patch. Considering a small window surrounding x_o, the gradient magnitude and orientation can be computed using finite differences. Local image patch orientation is then weighted by the corresponding magnitude and Gaussian window. Eventually the orientation is selected to be the peak of the weighted orientation histogram.

Building a nodule SIFT descriptor is similar to orientation assignment, for example a 16×16 image window surrounding the nodule centroid point is divided into sixteen 4×4 sub-windows, then an 8-bin weighted orientation histogram is computed for each sub-window, hence, $16 \times 8 = 128$ descriptors for each nodule is obtained. Thus, each detected nodule can now be defined at location (x_0, y_0), specific scale σ, explicit orientation θ and descriptor vector, $\mathrm{x}_o = \{\mathrm{x}_0, y_0, \sigma, \theta, \mathrm{d}\}$. Thus the SIFT operator $\mathcal{S} : \mathrm{I}(\mathrm{x}) \rightarrow \mathrm{X}$ can be viewed as mapping a CT slice I(x) to the nodule space with n-nodules, $\mathrm{X} = \{\mathrm{x_i}\}_{\mathrm{i}=1}^{\mathrm{n}}$ detected from I(x), where $\mathrm{x_i} = \left\{\mathrm{x}_0^{\mathrm{i}}, y_0^{\mathrm{i}}, \sigma_\mathrm{i}, \theta_\mathrm{i}, \mathrm{d_i}\right\}$. Principle component analysis (PCA) and linear discriminant analysis (LDA) are used to project the extracted SIFT descriptors to a low-dimensional subspace where noise is filtered out.

Example: Figure 16 shows four slices containing nodules <1 cm in size. The SIFT algorithm was applied to the four nodule types and the resulting discriptors were used to classify the nodules after a detection step, in order to reduce false positives. Small-size nodules lack textural distinction, but the shapes are distinct. Figure 17 shows the construction and values of the SIFT algorithm for the four nodule types. The values of the SIFT descriptor shows decent discrimination among the nodules.

5.2 Feature Distance Measures

The feature distance measurement is a numerical description of how far apart the feature vectors are from one another. Numerous methods found in the literature can be used; below are *described three different distance measurements.*

The Euclidean Distance: The Euclidian distance (ED) between feature point vectors ***p*** and ***t*** in the Euclidean n-space

$$\mathrm{ED} = \sqrt{\sum\nolimits_{\mathrm{i}=1}^{\mathrm{n}} (\mathrm{p_i} - \mathrm{t_i})^2} \tag{22}$$

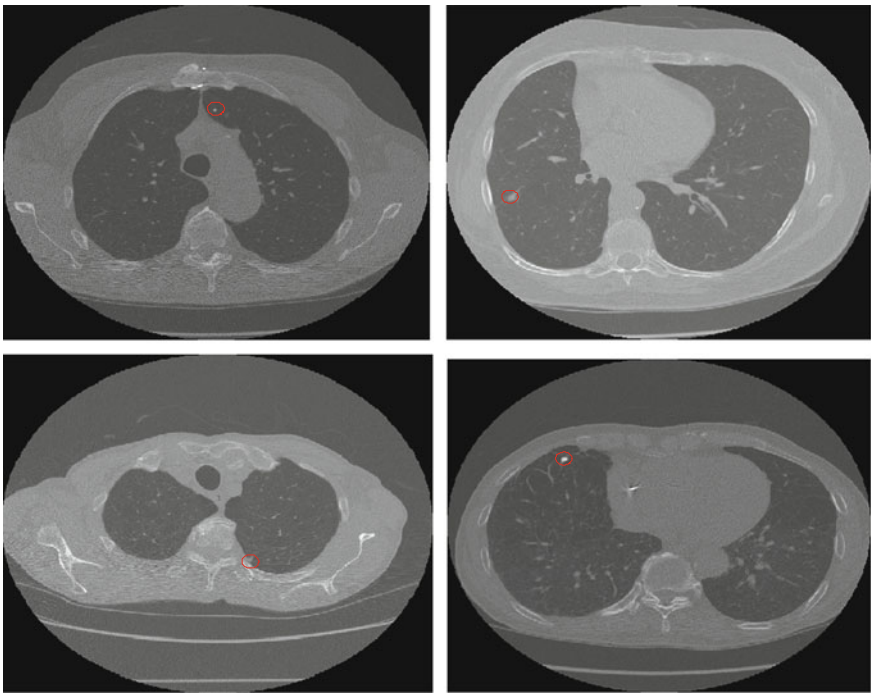

Fig. 16 Small-size lung nodules from LDCT scans. *Upper left* (well-circumscribed); *upper right* (vascular); *lower left* (juxta-pleural); *lower right* (pleural-tail). Nodules are marked by a *circle*

Note that the Euclidean distance is rotation invariant but not scale-invariant.

The Mahalanobis Distance: The Mahalanobis Distance is a scale-invariant distance measure based on correlations between variables by which variations can be identified for analysis. A multivariate vector $X = [x_1, x_2, \ldots, x_N]^T$ from a group of values with mean $\mu = [\mu_1, \mu_2, \ldots, \mu_N]^T$ and covariance matrix, S, is defined as:

$$D_M(\mathbf{X}) = \sqrt{(\mathbf{X} - \mu)^{\mathbf{T}} \mathbf{S}^{-\mathbf{1}} (\mathbf{X} - \mu)} \tag{23}$$

The Chebyshev Distance: This distance is a metric defined on a vector space where the distance between two vectors is the greatest of their differences along any coordinate dimension. The distance between two vector points P and t with standard coordinates p_i and t_i is defined as:

$$D_{\text{Chebyshev}}(\mathbf{p}, \mathbf{t}) = max\ (|p_i - t_i|) \tag{24}$$

Evaluation of these distance measures for shape analysis exist elsewhere (e.g., [30, 31]).

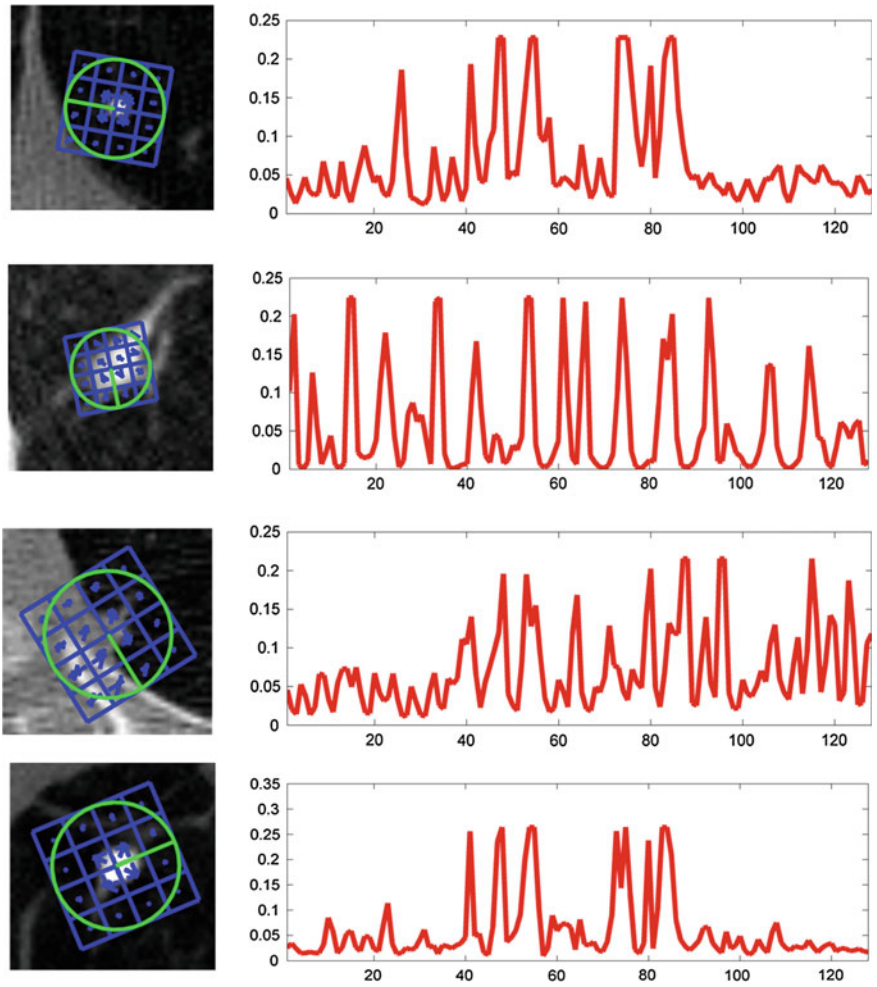

Fig. 17 SIFT desciptor applied to small-size nodule types in LDCT of the human chest. From top to bottom: well-cricumscribed, vascular, juxta-pleural and pleural-tails nodule types

5.3 Lung Nodule Classification

The above descriptors form the basis for the classification process to be examined in the following section.

5.3.1 General Approach

The general approach for nodule classification may be summarized by the following algorithm.

1. Construct a statistically sufficient database of pathological nodules;
2. Co-Register members of the nodule database to create the templates used for nodule detection, as described before;
3. Generate the feature vectors using the geometric descriptors (e.g., SIFT, ASFIT, SURF, LBP and Gabor Wavelet) for all members of the nodule database and store offline. Machine learning algorithms may be used such as PCA, RANSAC and Adaboost for optimal selections of the feature vector in terms of discrimination as well as execution time;
4. Perform the nodule detection using template matching;
5. Crop ROIs of sizes N $\times$ N over detected nodules (e.g., N=21)— these will be used for categorization;
6. Segment the nodule regions with the ROIs using the variational approach described in Chapter IV, enhanced with a priori information about shape and intensity, using the nodule database;
7. Repeat step #3 on the candidate nodules after segmentation; and
8. Calculate the distance between the feature vectors of candidate nodules and those in the pathological database, and assign the nodule category based on minimum distance.

The above algorithm may be carried out by various ways, depending the features available. Below feature-based and registartion-based nodule classifcation implemented in the author's recent work [23, 27] are discussed.

5.3.2 Feature-Based Classification

The most significant classification results were obtained when the shape based signed distance transform was combined to the texture based LBP approach. The results in Tables 1, 2, 3 illustrate the classification results of the signed distance transform versus the multi-resolution local binary pattern (LBP). A third feature descriptor using the combination of the methods is also shown.

Higher true-positive rates can be seen from the LDA projection in Tables 1 and 2 when more training is conducted using either the LBP or distance descriptors separately. When comparing the PCA results less training data resulted in better true-positive classification of nodules. In the non-nodule distance transform experimentations more training data was needed to obtain in some instances perfect results. This is understandable since the non-nodules do not have specific shape characteristics that can be defined or manipulated as in the nodules case.

Overall, the PCA combinational shape and feature description of nodules resulted in a drastic true-positive rate increase in classification. All of the results depicted in Tables 1 and 2 allow the conclusion to be made that non-nodules do in-fact contain

Table 1 Classification results for various nodules using raw LBP, LDA LBP and PCA LBP with variable training percentages

Nodule type	Raw LBP				LDA LBP				PCA LBP			
	100 %	75 %	50 %	25 %	100 %	75 %	50 %	25 %	100 %	75 %	50 %	25 %
Juxta pleural	52	50	47	38	100	86	65	50	64	64	59	67
Well-circumscribed	40	41	40	26	65	80	63	36	64	60	66	82
Vascular	22	29	32	10	32	76	56	32	20	22	37	56
Pleural tail	22	20	17	11	100	76	52	39	33	17	33	46
Non nodule	78	77	74	68	100	88	60	44	86	87	83	96

Table 2 Classification results for various nodules using raw distance transform, LDA LBP and PCA distance transform with variable training percentages

Nodule type	Raw distance transform				LDA distance transform				PCA distance transform			
	100 %	75 %	50 %	25 %	100 %	75 %	50 %	25 %	100 %	75 %	50 %	25 %
Juxta pleural	38	39	35	34	100	88	61	45	62	54	60	68
Well-circumscribed	33	33	36	34	74	83	63	45	46	59	48	55
Vascular	12	12	15	15	29	76	54	29	37	22	61	63
Pleural tail	17	17	17	15	100	85	54	33	17	24	35	52
Non nodule	63	68	68	49	100	87	65	49	83	89	85	79

Table 3 Classification results obtained from raw combinational feature transform and PCA combinational feature transform with variable training percentages

Nodule Type	Raw combinational feature descriptor				PCA on combinational feature descriptor			
	100 %	75 %	50 %	25 %	100 %	75 %	50 %	25 %
Juxta Pleural	40	41	39	37	78	76	76	79
Well-circumscribed	40	37	36	34	73	68	71	68
Vascular	24	20	22	12	51	54	44	76
Pleural tail	22	26	22	20	33	35	41	54
Non nodule	63	57	58	49	100	99	100	98

descriptor variations that allow them to be correctly classified. Also, combination of shape and texture feature information allows for better object representation to be obtained, thus improved results in classification.

Table 3 depicts impressive results when the LBP was obtained from the distance transform images. A 20 % true-positive rate increase was found, in the PCA 25 % training combinational vascular nodule case when comparing it to the PCA LBP results obtained when only the texture information was used for classification, and a 13 % increase over the distance transform results alone. Variations of percentage increases were seen for each nodule category.

5.3.3 Registration-Based Classification

The idea of the registartion-based classification is to compare the segmented nodules with nodule models, using a registration algorithm. Since the AAM approach generated impressive nodule models, which resembled both the shape and appreance of real nodules, it is plausible to use the normalized nodule models as templates to compare with candidate nodules for classifcation. From the face recognition analogy, a probe (test face) is compared to a gallary using either direct matching (by registration) or through the use of features.

The following terminologies are relavant to the categorization process:

(i) *Target* set $\mathcal{T}$: a set of textured regions containing the nodule models generated by the deformable model approach for all nodule types.
(ii) *Gallery* set $\mathcal{G}$: a subset of $\mathcal{T}$ containing template(s) to be matched in a certain matching setup.
(iii) *Query* set $\mathcal{Q}$: a set of textured regions of unknown nodule type, where nodule type identification is performed by matching all elements in the query set to the target set.
(iv) *Probe* set $\mathcal{P}_{\mathcal{G}}$:a subset of $\mathcal{Q}$, where each element has a match in the gallery set.
(v) *Imposter* set $\mathcal{P}_{\mathcal{N}}$: a subset of $\mathcal{Q}$, which contains elements that don't have a match in the gallery set.

As an example, again, using the face recognition terminology, a region centered at a well circumscribed nodule is considered an imposter to a gallery containing only juxta pleural nodules. Also a non-nodule region is always considered as an imposter. Comparing the feature vector for all nodule models in the gallery set with the feature vector for all regions in the probe set results in a similarity matrix $\mathcal{S}$, where the ijth element is the similarity between the ith element of the gallery and the jth element of the probe. The following metrics can be defined according to a similarity score: Normalized cross-corerlation (NCC), the mutual information (MI) or the output of descriptors such as SFIT, LBP, etc.

Identification Rate/Probability: It is calculated as the proportion of testing nodules correctly matched to its own type, i.e. probe $\mathrm{P_j}$ is identified correctly in the top N gallery nodule types, where $\mathrm{N} = \mathrm{renk}(\mathrm{P_j})$, such that:

$$\mathrm{rank}\left(\mathrm{p_j}\right) = \left|\left\{\mathrm{g_k} : \mathrm{s_{kj}} \geq \mathrm{s_{ij}},\ \mathrm{id}\left(\mathrm{g_i}\right) = \mathrm{id}\left(\mathrm{p_j}\right)\right\}\right| \qquad \forall \mathrm{g_k}, \mathrm{g_i} \in \mathcal{G} \tag{25}$$

For each probe in the probe set , the similarity measures are sorted against the gallery, and obtain the rank of the match. Identification performance is then stated as the fraction of probes whose gallery match is at rank or lower. Thus the probability of identification at specific rank is defined as:

$$\mathrm{P_I}\left(\mathrm{r}\right) = \frac{\left|\left\{\mathrm{p_j} : \mathrm{rank}\left(\mathrm{p_j}\right) \leq \mathrm{r}\right\}\right|}{\left|\mathcal{P}_{\mathcal{G}}\right|} \qquad \forall \mathrm{p_j} \in \mathcal{P}_{\mathcal{G}} \tag{26}$$

Table 4 Results of the nodule categorization using registration/matching nodule candidates to nodule models

Nodule model	Nodule and background				Nodule region segmented			
	Rank 1	Rank 2	Rank 3	Rank 4	Rank 1	Rank 2	Rank 3	Rank 4
Juxtal pleural	0.4606	0.9217	0.9826	1.0	0.4261	0.9217	0.9826	1.0
Well-circumscribed	0.764	0.7978	0.8427	1.0	0.8876	0.9663	0.9775	1.0
Vascularized	0.4146	1.0	1.0	1.0	0.5122	1.0	1.0	1.0
Pleural tail	0.3261	0.7609	0.8261	1.0	0.3913	0.5217	0.5435	1.0

These quantities have been calculated for all the nodules in the ELCAP data. Table 4 shows the results for the four nodule categories.

In measuring the ranking, the cropped nodules are used in two fashion; without segmentation (i.e., no extraction of the nodule part in the cropped region) and with segmentation. The segmentation of nodules were conducted by various homegrown methods (including use of shape and intensity priors in an energy model optimized by graph cuts; also experimented with were basic segmentation using adaptive thresholding of the cropped regions by median filtering and anisotropic diffusion filtering, etc.).

Figure 18 is the ROC for 291 nodules specified in the ELCAP dataset. Both the well-circumscribed and the viscularized nodules provide the best performance. This is because both nodule types possess the best texture and shape information that enhances the correlation between the nodules and the models.

In general, the results of the ranking (i.e., matching models with nodules) improved by segmentation of the nodule portion in the cropped region. Model-based approaches such level sets and combinations of Gibbs-Markov models enhance the segmentation at severe computation cost. Nodule segmentation is a work in progress issue. A code or signature for the models and the nodules will provide better matching than using the classic image registration methods on regions with small spatial support. The conclusion, however is that the cropped regions have always been correctly categorized within second ranks by a simple computational approach such the normalized cross-correlation. This indeed is very encouraging for moving into using context based image processing and the ability to invoke advanced machine learning approaches to perform the matching process.

The extensive analysis using the approaches described in this chapter has allowed several conclusions to be made:

(1) Texture and shape feature information separately are not sufficient for lung nodule categorization, since the combination of the approaches yielded great improvements.
(2) In all of the approaches used, the non-nodule features generated and projected by PCA or LDA provided excellent classification results; thus, non-nodules contain descriptor variations that allow them to be correctly classified and not confused with nodules.

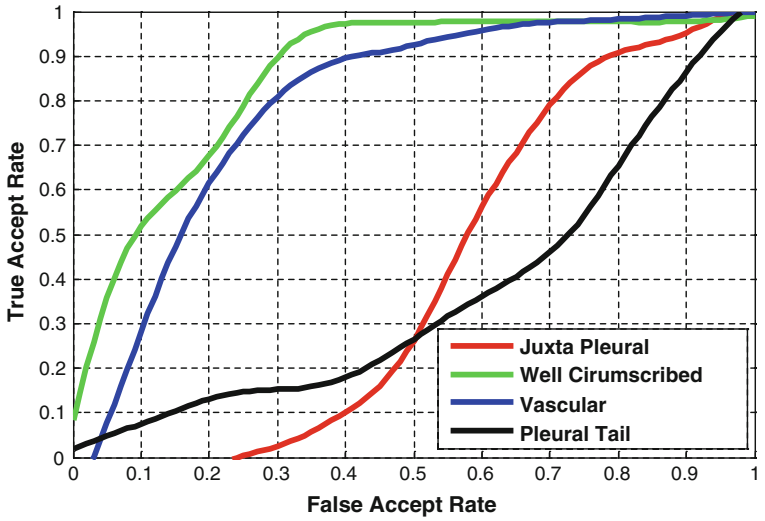

Fig. 18 ROC of automatic categorization on the ELCAP data. Well-circumscribed and vascular nodule types possess the best ranking for automatic categorization

(3) Intensity-based registration methods did not provide accurate categorization of small objects; a more appropriate similarity measures may be needed for these types of objects.
(4) Signatures of nodules—based on multiple approaches—may be generated and used for categorization; similar to face recognition methods. However, more extensive annotated databases of nodules are needed.

5.4 Summary

In this chapter, a system for nodule candidate detection and classification was created to show the robustness and accuracy of the produced models. Detection using a template matching method with normalized cross-correlation similarity measure without false positive reduction was implemented to show the robustness of the data-driven templates formulated from the AAM and ASM approaches over the known parametric template generation. Detection using the data driven template matching approach, after false positive reduction via SIFT and LBP feature extraction, was also implemented, further enhancing the detection process.

Classification of the nodules and non-nodules were examined using a k-NN leave-one-out algorithm with the Euclidean distance as the similarity measure, in order to test whether or not significant distinctions between the nodule classes exist. An overall 12% true-positive rate increase was found in the PCA combinational classification results over using the PCA LBP or the PCA distance transform separately. Various extensions and detailed analysis of biomedical imaging can be found in Farag [31].

References

1. Kostis WJ et al (2004) Small pulmonary nodules: reproducibility of three-dimensional volumetric measurement and estimation of time to follow-up. Radiology 231:446–52
2. Farag AA (2009) Lung nodule modeling and detection for computerized image analysis of low dose CT imaging of the chest. Master of Engineering, University of Louisville
3. ELCAP public lung image database. www.via.cornell.edu/databases/lungdb.html
4. Armato G, McLennan G, McNitt-Gray MF, Meyer CR, Yankelevitz D, Aberle DR, Henschke CI, Hoffman EA, Kazerooni EA, MacMahon H, Reeves AP, Croft BY, Clarke LP (2004) Lung image database consortium: developing a resource for the medical imaging research community. Radiology 232(3):739–748
5. Kendall DG (1984) Shape manifolds, procrustean metrics, and complex projective spaces. Bull Lond Math Soc 16(2):81–121
6. Julesz B et al (1973) Inability of humans to discriminate between visual textures that agree in second-order statistics-revisited. Perception 2:391–405
7. Dryden IL, Mardia KV (1998) Statistical shape analysis. John Wiley & Sons, New York
8. Cootes TF, Taylor CJ (2004) Anatomical Statistical Models and their role in feature extraction. Br J Radiol 77:S133–S139
9. Mathews I, Baker S (2004) Active appearance models revisited. Int J Comput Vision 60(2):135–164
10. Farag AA, Graham J, Farag AA, Elshazly S, Falk R (2010) Parametric and non-parametric nodule models: design and Evaluation. Workshop on pulmonary image processing in conjunction with MICCAI-10, Beijing, pp 151–162
11. Farag AA, Abdelmunim H, Graham J, Farag AA, Carter C, Elshazly S, El-Mogy S, El-Mogy MS, Falk R (2012) An AAM-based approach for lung nodule detection from low dose CT (LDCT) scans, International symposium on biomedical imaging (ISBI 12), Barcelona, Spain, pp 1040–1043
12. Farag AA (2013) A variational approach for small-size lung Nodule segmentation. International symposium on biomedical imaging (ISBI 13), San Francisco, CA, pp 81–84
13. Zhao B, Yankelevitz D, Reeves A, Henschke C (1999) Two-dimensional multi-criterion segmentation of pulmonary nodules on helical CT images. Med Phys 26(6):889–95
14. Ko JP, Rusinek H, Jacobs EL, Babb JS, Betke M, McGuinness G, Naidich DP (2003) Small pulmonary nodules: volume measurement at chest CT-phantom study. Radiology 228(3):864–870
15. Kuhnigk JM, Dicken V, Bornemann L, Bakai A, Wormanns D, Krass S, Peitgen HO (2006) Morphological segmentation and partial volume analysis for volumetry of solid pulmonary lesions in thoracic CT scans. IEEE Trans Med Imaging 25(4):417434
16. Kubota T, Jerebko AK, Dewan M, Salganicoff M, Krishnan A (2011) Segmentation of pulmonary nodules of various densities with morphological approaches and convexity models. Med Image Anal 15(1):133–154
17. Dijia Wu, Le Lu, Jinbo Bi, Shinagawa Y, Boyer KL, Krishnan A, Salganicoff1 M (2010) Stratified learning of local anatomical context for lung nodules in ct images. The twenty-third IEEE conference on computer vision and pattern recognition, CVPR 2010, San Francisco, California, USA
18. Armato SG 3rd, Giger ML, Moran CJ, Blackburn JT, Doi K (1999) MacMahon H (1999) Computerized detection of pulmonary nodules on CT scans. J Radio Graph 19:1303–1311
19. Diciotti Stefano, Lombardo Simone, Falchini Massimo, Picozzi Giulia, Mascalchi Mario (2011) Automated segmentation refinement of small lung nodules in CT scans by local shape analysis. IEEE Trans Biomed Eng 58(12):3418–3428
20. Diciotti Stefano, Picozzi Giulia, Falchini Massimo, Mascalchi Mario, Villari Natale, Valli Guido (2008) 3-D segmentation algorithm of small lung nodules in spiral CT images. IEEE Trans Inf Technol Biomed 12(1):7–19

21. Munim HAE, Farag AA (2007) Curve/surface representation and evolution using vector level sets with application to the shape-based segmentation problem. IEEE Trans Pattern Anal Mach Intell 29(6):945–958
22. Farag A, Graham J, Farag A (2010) Robust segmentation of lung tissue in chest CT scanning. Proceedings of the 2010 IEEE international conference on image processing (ICIP), pp 2249–2252
23. Farag AA (2012) Modeling small objects under uncertainties: novel algorithms and applications. CVIP Lab, Ph.D. Dissertation, University of Louisville
24. Ojala T, Pietikainen M, Maenpaa T (2002) Multiresolution gray-scale and rotation invariant texture classification with local binary patterns. IEEE Trans Pattern Anal Mac Intell 24:971–987
25. Lowe DG (2004) Distinctive image features from scale-invariant keypoints. Int J Comput Vis 60(2):91–110
26. Mikolajczyk K, Schmid C (2005) A performance evaluation of local descriptors. IEEE Trans Pattern Anal Mac Intell 27(10):1615–1630
27. Farag AA, Elhabian S, Graham J, Farag AA, Falk R (2010) Toward precise pulmonary nodule descriptors for nodule type classification. Proceedings of the 13th international conference on medical image computing and computer assisted intervention (MICCAI), pp 626–633
28. Koenderink JJ (1984) The structure of images. Biol Cybern 50:363–396
29. Lindeberg T (1993) Detecting salient blob-like image structures and their scales with a scale-space primal sketch: a method for focus-of-attention. Int J Comput Vis 11(3):283–318
30. Duda RO, Hart PE, Stork DG (2001) Pattern classification, 2nd edn. Wiley, New York
31. Farag Aly (2013) Biomedical image analysis: statistical and variational approaches. Cambridge University Press, Cambridge